

Manuscript version: Author's Accepted Manuscript

The version presented in WRAP is the author's accepted manuscript and may differ from the published version or Version of Record.

Persistent WRAP URL:

<http://wrap.warwick.ac.uk/158214>

How to cite:

Please refer to published version for the most recent bibliographic citation information. If a published version is known of, the repository item page linked to above, will contain details on accessing it.

Copyright and reuse:

The Warwick Research Archive Portal (WRAP) makes this work by researchers of the University of Warwick available open access under the following conditions.

© 2021 Elsevier. Licensed under the Creative Commons Attribution-NonCommercial-NoDerivatives 4.0 International <http://creativecommons.org/licenses/by-nc-nd/4.0/>.



Publisher's statement:

Please refer to the repository item page, publisher's statement section, for further information.

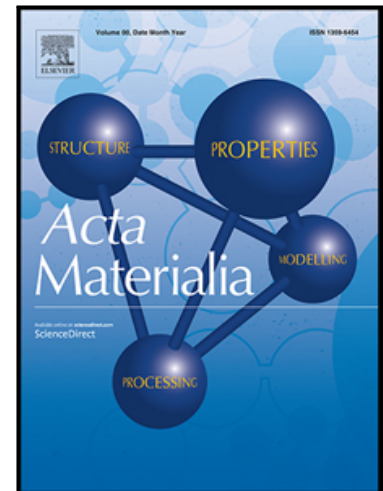
For more information, please contact the WRAP Team at: wrap@warwick.ac.uk.

Journal Pre-proof

Nitrogen diffusion in vacancy-rich ferrite and austenite, from first principles to applications

Aurash Karimi, Michael Auinger

PII: S1359-6454(21)00672-8
DOI: <https://doi.org/10.1016/j.actamat.2021.117292>
Reference: AM 117292



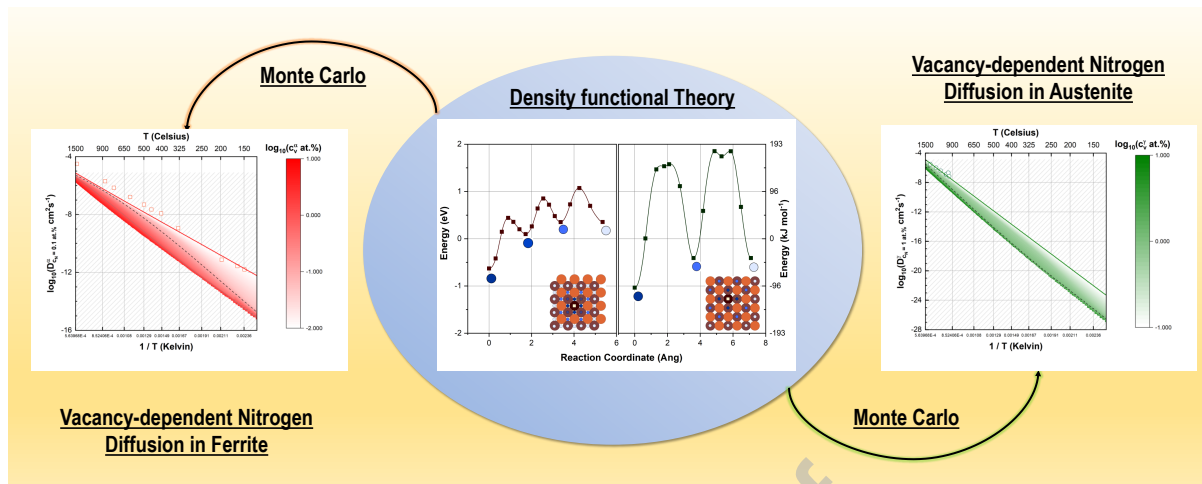
To appear in: *Acta Materialia*

Received date: 4 September 2020
Revised date: 28 August 2021
Accepted date: 1 September 2021

Please cite this article as: Aurash Karimi, Michael Auinger, Nitrogen diffusion in vacancy-rich ferrite and austenite, from first principles to applications, *Acta Materialia* (2021), doi: <https://doi.org/10.1016/j.actamat.2021.117292>

This is a PDF file of an article that has undergone enhancements after acceptance, such as the addition of a cover page and metadata, and formatting for readability, but it is not yet the definitive version of record. This version will undergo additional copyediting, typesetting and review before it is published in its final form, but we are providing this version to give early visibility of the article. Please note that, during the production process, errors may be discovered which could affect the content, and all legal disclaimers that apply to the journal pertain.

© 2021 Published by Elsevier Ltd on behalf of Acta Materialia Inc.



Journal Pre-proof

Nitrogen diffusion in vacancy-rich ferrite and austenite, from first principles to applications

Aurash Karimi^{a,*}, Michael Auinger^{a,*}

^aWMG, University of Warwick, Coventry CV4 7AL, United Kingdom

Abstract

This work contains a systematic study of the diffusion of nitrogen in Ferrite (α Fe) and Austenite (γ Fe) from first principles, using a robust multiscale model which combines Density Functional Theory (DFT) and Kinetic Monte Carlo (KMC). Both ferromagnetic BCC Fe and non-magnetic FCC Fe are considered using DFT to drive a diffusion model, which shows strong agreement with experimental diffusion data in literature. Further, quantified predictions are calculated for nitrogen diffusion in iron crystals which are vacancy-rich. It was found that an extended diffusion coefficient of nitrogen can be expressed as a function of nitrogen and vacancy concentration by fitting polynomial coefficients. These are calculated within the $100^\circ\text{C} < T < 1538^\circ\text{C}$ temperature range, and $0.1 \text{ at.}\% < c_N < 1 \text{ at.}\%$ nitrogen concentration range. Moreover, the error of extrapolating the diffusion coefficient outside of the calculated nitrogen concentration range was found to be small at some temperatures. Such insights in vacancy-rich crystals may be useful to nitriding manufacturers, as enhanced diffusion models are an important factor in improving existing processes and avoiding common manufacturing problems such as the *egg-shell-effect*.

Keywords: A. Modeling, B. Ab initio calculations, C. MC simulations, D. Vacancies, E. Nitriding

1. Introduction

Nitriding is used to increase the mechanical strength and wear resistance of metallic work pieces such as cutting blades, gearwheels and crankshafts. Conventional nitriding processes such as gas nitriding and plasma nitriding, use the surface adsorption and subsequent diffusion of nitrogen atoms to form a hard surface layer (termed "compound layer") that is composed of ϵ and γ' -type iron nitrides. The resulting surface is often brittle, causing the material to form cracks upon impact, which leads to spallation of the surface layer. To prevent this so called *egg-shell-effect* [1, 2], a "diffusion layer" or "hardness transition zone" which contains α and/or γ -type nitrides should be formed underneath the compound layer, where the hardness profile gradually decreases from the surface level towards the interior. Anticipating the composition and depth of the diffusion layer is therefore vital to the heat treatment process.

To enhance the predictive capability of diffusion layer growth models, nitrogen diffusion in α and γ Fe is revisited in this work from first principles using Density Functional Theory (DFT) and Kinetic Monte Carlo (KMC). Ferromagnetic body-centered cubic (BCC) and non-magnetic face-centered cubic (FCC) iron lattices are used to represent high purity α and γ Fe respectively. By their design, DFT calculations most accurately depict idealised (perfectly symmetrical) crystal structures, while industrial iron alloy grades inevitably contain numerous atomic-scale defects. There is evidence that this distinction between DFT and iron alloys in reality is significant when making thermodynamic predictions from first principles. For example, it has been shown that DFT-calculated nitrogen solubility's in iron have closer agreement with experimental data when excess vacancies [3] are introduced to idealised lattices. Furthermore, common processes encountered in industry; such as irradiation [4, 5], quenching [6], ball milling and shot peening [7]; lead to deformed lattices which further increase nitrogen-vacancy interactions. Thus, the diffusion

*Corresponding authors

Email addresses: a.karimi@warwick.ac.uk (Aurash Karimi), m.auinger@warwick.ac.uk (Michael Auinger)

of nitrogen is considered in both idealised and vacancy-rich BCC/FCC lattices. This work attempts to exhaustively consider the range of vacancy concentrations which would impact nitrogen diffusion in a meaningful way during heat treatment. However, experimental evidence is required to verify whether the levels of deformation (up to 10 at.% vacancies) which are considered occur in applied contexts.

Many sources [8, 9] report that the energy barrier for nitrogen diffusion obtained by DFT calculations using ferromagnetic BCC iron has strong agreement to the low-temperature energy barrier obtained from experimental data for α Fe [10]. The situation is more challenging for γ Fe since it is both unstable at low temperatures (at high Fe purity) and paramagnetic, which are not readily incorporated features in DFT modelling. Anti-ferromagnetic FCC models are commonly used as they yield energy barriers close to that of solute-rich (expanded) austenite, which are typically around $0.8 \text{ eV} = 77.2 \text{ kJ mol}^{-1}$ [11, 12]. However, there is limited DFT literature which investigates the dilute-solute case, which is known experimentally to have a distinctly larger energy barrier for diffusion $1.74 \text{ eV} = 167 \text{ kJ mol}^{-1}$ [13]. Both nitrogen [14] and carbon [15] energy barriers are found to be consistently overestimated from DFT calculations using non-magnetic FCC iron, exceeding their experimental evaluations by more than $0.5 \text{ eV} = 48.2 \text{ kJ mol}^{-1}$. Discrepancies of this magnitude are peculiar, since at temperatures where austenite is in thermodynamic equilibrium, the magnetic contribution to diffusion energy barriers should be relatively small. To investigate, a non-magnetic FCC model which incorporates temperature dependent factors such as thermal expansion and vibrational energy is considered in this work.

In previous DFT literature, the energy barriers for nitrogen diffusion in the proximity of vacancies have been explored for both ferromagnetic BCC [16] and anti-ferromagnetic FCC [14] iron. Moreover, experimental approaches such as resistivity recovery [17] and irradiation [18] have been used to calculate nitrogen-vacancy trapping enthalpies in α Fe. Hence, it is well established that vacancies act as trapping sites for diffusing nitrogen, leading to the formation of nitrogen-vacancy complexes. Historically, it has been assumed for modelling purposes that the impact of vacancies on nitrogen diffusivity could be calculated as a function of the trapping enthalpy only. More recent approaches improve on this assumption by using multiscale modelling to incorporate more intricate details calculated from first principles [16, 19]. However, state of the art models which take advantage of the increasing supply of highly refined first principles data generated by DFT studies are rarely used in applied contexts. The aim of this work is to help bridge this gap by focusing foremost on accessibility of the modelling results and comparisons with experimental data. The impact of vacancies on nitrogen diffusion is quantified, in both α and γ Fe, by simulating nitrogen diffusion in a range of nitrogen concentrations c_N , vacancy concentrations c_v and temperatures T . The simulation results are used to fit polynomial expressions, allowing experimentalists to access quantitative data on the nitrogen diffusion coefficients as a function of c_N , c_v and T .

2. Methods

First principles data calculated as outlined in section 2.1 is used in combination with published data from [3] to calculate the jump rates for diffusion (see section 2.2.1) in BCC/FCC iron containing vacant lattice sites and interstitially dissolved nitrogen. Section 2.1 features only new/essential details regarding the DFT methodology applied, the reader is referred to the previously published work mentioned for more detailed discussion. In particular, the energy barriers for nitrogen jumps in the proximity of a vacancy are quoted from [3] in table 2, which are needed to calculate the jump rates defined in equation 3. Using the calculated jump rates, an array of KMC trajectories are used to study the dynamics of the iron-vacancy-nitrogen system over the chosen temperature and nitrogen/vacancy concentration ranges. As detailed in 2.2.2, the data from trajectories are used to create polynomial expressions for the diffusion coefficient of interstitial nitrogen atoms.

2.1. First Principles Calculations

The projector augmented wave method as implemented in GPAW [20, 21], applying the exchange correlation functional [22] of Perdew, Burke and Ernzerhof (PBE), was used in for all DFT calculations. Atomic Simulation Environment (ASE) [23] was used to interact with the GPAW software. The parameters which are chosen for each DFT calculation are adapted from previous work [3]. These are the kinetic cut-off energy for plane-wave functions, the number of k-points distributed in the Brillouin zone using the Monkhorst-Pack method [24], the supercell size, and the width of Methfessel-Paxton [25] (first order) smearing. The smearing width is set to 0.1 for all calculations. All

other DFT parameters, which were chosen from their convergence behaviour with respect to the two (ferromagnetic BCC and non-magnetic FCC) Fe systems of interest, are specified in table 1. The uncertainty estimates are calculated by summing together the residual error margins of the cut-off energy, the supercell size, and the number of k-points. The residual error margins are calculated as the energy difference between the last two iterations of the convergence test for each DFT parameter with respect to the calculated DFT energy.

Table 1: Parameter sets used for all plane wave DFT calculations in this work, for supercells of BCC/FCC Fe containing nitrogen and/or vacancies. The estimated uncertainty in energy barriers calculated using these parameters is included from [3].

| Lattice | E_{cut} (eV) | Supercell Size | K-points | Uncertainty (eV) |
|---------------------|-----------------------|-----------------------|-----------------------|------------------|
| BCC (ferromagnetic) | 500 | $3 \times 3 \times 3$ | $8 \times 8 \times 8$ | 0.010 |
| FCC (non-magnetic) | | $3 \times 2 \times 2$ | $6 \times 8 \times 8$ | 0.036 |

The Nudged elastic band (NEB) [26] method was used to calculate minimum energy pathways (and subsequently the energy barriers) for nitrogen and iron atoms transitioning between interstitial sites and lattice sites respectively. In all cases the NEB images are relaxed with the Broyden-Fletcher-Goldfarb-Shanno (BFGS) algorithm as implemented in Atomic Simulation Environment [23] (ASE) until the overall forces were less than 0.5 eV, then climbing image NEB [27] is used with the FIRE algorithm [28] until the forces are less than 0.025 eV.

Using the location of transition states which are obtained using NEB results, the volume dependencies of energy barriers for nitrogen are calculated by fixing two iron atoms in supercells containing nitrogen in both transition and octahedral positions. The supercells are held at fixed volume over a range of evenly spaced lattice parameters up to 5.46% (BCC) and 4.70% (FCC) larger than their (DFT calculated) equilibrium values. At each volume, the supercell is relaxed with BFGS.

Vibrational frequencies are calculated for the nitrogen atom in octahedral and transition sites, where it is treated as an independent three-dimensional harmonic oscillator. The nitrogen atom is displaced by 0.01 Å in six Cartesian directions to assemble a Hessian matrix using the central differences method. Three frequencies are calculated, which are used in equation 1 to calculate the temperature-dependent Helmholtz energy $E(T)$ from the corresponding ground state energy E :

$$E(T) = E + E_{\text{zpe}} + \sum_i^{i=3} k_{\text{B}} T \ln(1 - e^{-\frac{\epsilon_i}{k_{\text{B}} T}}) \quad (1)$$

Where the ϵ_i are the energy associated with each vibrational frequency, E_{zpe} is the zero-point energy and k_{B} is the Boltzmann constant. The volume dependence and the vibrational frequencies are calculated using the same DFT parameters which were used in NEB calculations (see table 1). It was assumed that calculating volume dependence and vibrational frequencies for vacancy-containing supercells is not impactful enough in diffusion modelling to justify the computing resources required, so only the ideal (vacancy-free) case is considered for these contributions.

The repulsion energy of diffusing nitrogen atoms $E_{\text{N-N}}$ is approximated using the nitrogen binding energy of a supercell containing two neighbouring nitrogen atoms. Let $\tilde{E}(X)$ denote the ground state energy of X calculated in a DFT supercell, then:

$$E_{\text{N-N}} = \tilde{E}(\text{Fe}_n\text{N}_2) - \tilde{E}(\text{Fe}_n\text{N}) - \frac{1}{2}\tilde{E}(\text{N}_2) \quad (2)$$

where n is the amount of iron atoms in the supercell.

2.2. Diffusion Model

2.2.1. Jump Rates

The energy barrier for a diffusing species x with an interacting neighbour species y to jump to a new stable position is denoted by $E_{y(i \rightarrow j)}^x$, where the old (pre-jump) and new position of x are i 'th and j 'th nearest neighbours to y . In this work only nitrogen and vacancies are considered, so $x, y \in \{\text{N}, \text{v}\}$ where "v" denotes a vacancy. The third ($i, j < 4$) and second ($i, j < 3$) nearest neighbours are the farthest interactions considered for BCC and FCC Fe respectively, as these constraints are considered to be a good compromise between computational burden and accuracy [3]. The

nearest neighbour positions and jump paths for a nitrogen atom in the proximity of a vacancy are shown in figure 1. The isolated and dilute energy barrier is denoted $E_{y(\infty \rightarrow \infty)}^x := \Delta E^x$, where x is the diffusing species. In the FCC crystal, it is approximated that $E_{v(2 \rightarrow 2)}^N = \Delta E^N$. This is because the vacancy is too far away to have a significant effect on the energy barrier for the $2 \rightarrow 2$ jump [3]. The variant of KMC used in this work does not efficiently simulate diffusion within deep energy basins i.e. the FCC $1 \rightarrow 1$ jump. Whilst modifications to the KMC algorithm have recently been demonstrated to accelerate convergence in this situation [29, 30, 31], the FCC $1 \rightarrow 1$ jump is omitted in the present diffusion simulations. As detailed in Appendix A, the contribution of the $1 \rightarrow 1$ jumps to the calculated macroscopic diffusion coefficient of nitrogen is small enough to justify their omission.

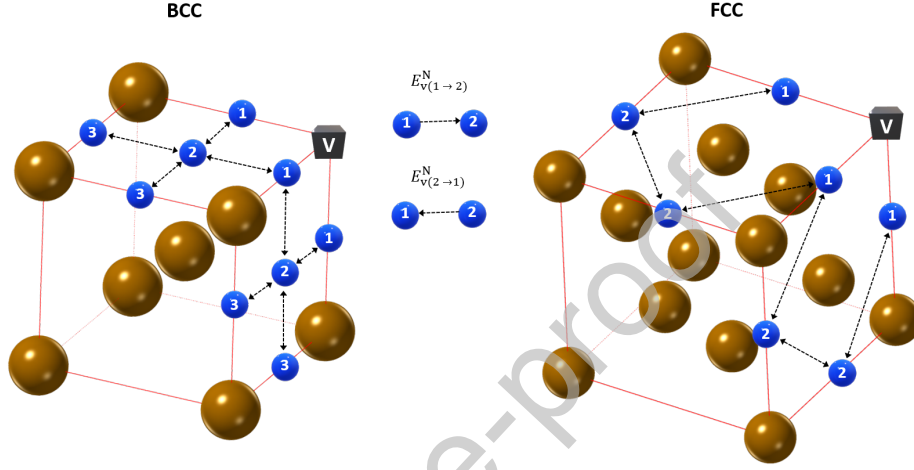


Figure 1: Jump paths (black arrows) and interstitial positions (blue spheres) for a nitrogen atom in nearest neighbour positions around a vacancy (grey cube) in BCC and FCC lattices. A numbering of i indicates that an interstitial position is an i 'th nearest neighbour to the vacancy. $E_{y(i \rightarrow j)}^N$ denotes the energy barrier for nitrogen to jump from an i position to a j position.

A jump rate $r_{y(i \rightarrow j)}^x$ of x is defined for each unique energy barrier of x at temperature T by the equation

$$r_{y(i \rightarrow j)}^x(V, T) = \nu_x e^{-\frac{E_{y(i \rightarrow j)}^x(V, T) + E_{N-N}^*(x)}{RT}} \quad (3)$$

$$E_{N-N}^*(x) = \begin{cases} (\text{Number of nearest-neighbour N adjacent to jump destination}) \times E_{N-N} & x = N \\ 0 & \text{otherwise} \end{cases} \quad (4)$$

Where $R = 8.314 \text{ J mol}^{-1} \text{ K}^{-1}$ is the universal gas constant. Experimental data [32] of lattice expansion with respect to temperature is combined with calculated data of energy barriers at expanded supercell volumes (see section 2.1), to account for the impact of thermal expansion on nitrogen diffusion. Consequently, the volume dependence of each $E_{y(i \rightarrow j)}^N(V, T)$ used in equation 3 is reduced to a temperature dependence in practice. Moreover, $E_{y(i \rightarrow j)}^N(V, T)$ contains the temperature dependent vibrational contributions shown in equation 1. The attempt frequency of nitrogen jumps ν_N is calculated from DFT, by dividing the product of vibrational frequencies of nitrogen in an octahedral site by the product of the vibrational frequencies in the corresponding tetrahedral transition site (omitting the weakest frequency at the tetrahedral site). The $E_{N-N}^*(x)$ term defined in equation 4 is used to account for nitrogen repulsion. The repulsion energy adjusts the rate at which nitrogen atoms jump to a nearest neighbour position of other nitrogen by the proportion of paired N-N complexes relative to lone nitrogen interstitials at equilibrium (see equation 2). Due to the way it is defined, the repulsion contribution only applies when nitrogen has a candidate jump which is already the nearest neighbour to one or more other nitrogen atoms. Furthermore, if the jump is in the range of a vacancy, it is approximated that the vacancy does not influence the repulsion energy.

To calculate the jump rate $r_{y(i \rightarrow j)}^x$ for each x to jump from its current position to a candidate position, the nearest neighbour distances of both positions to the closest y are considered. For example, suppose $x = N$ and $y = v$. If the

closest vacancy to the nitrogen atom in its current position is a second nearest neighbour ($i = 2$) and the candidate position is a first nearest neighbour to the vacancy ($j = 1$), then the rate for nitrogen to jump to the candidate position is given by $r_{v(2 \rightarrow 1)}^N(T)$.

2.2.2. Diffusion Coefficient

At temperature T , the interstitial diffusion coefficient D^s of nitrogen atoms dissolved in iron containing vacancy and nitrogen concentrations of c_v and c_N respectively, is defined for considered phases of iron $s \in \{\alpha, \gamma\}$ by the equation

$$\ln(D^s(T, c_v, c_N)) = \sum_{k=0}^{k \leq 3} a_k^s \left(\frac{1}{T}\right)^k. \quad (5)$$

By employing the jump rates which are calculated as outlined in section 2.2.1, the KMC algorithm as implemented in [33] is used to generate trajectories of mobile nitrogen atoms within $25 \times 25 \times 25$ supercells of BCC Fe (31 250 atoms) and FCC Fe (62 500 atoms). Let T_m , c_{vm} and c_{Nm} represent the fixed conditions of the KMC supercell for each independent and unique trajectory, indexed by m . Let $x_n(t)$ denote the position of nitrogen atom n at time t within a KMC simulation cell containing a total of N mobile nitrogen atoms. The value of the diffusion coefficient (equation 5) for each m is given from a KMC trajectory by calculating the mean squared displacement (MSD)

$$\mu_N(t, T_m, c_{vm}, c_{Nm}) = \sum_{n=1}^N \frac{|x_n(t) - x_n(0)|^2}{N}. \quad (6)$$

Where

$$D^s(T_m, c_{vm}, c_{Nm}) = \lim_{t \rightarrow \infty} \frac{\mu_N(t, T_m, c_{vm}, c_{Nm})}{6t}. \quad (7)$$

The evolution of the MSD (equation 6) as time passes in the KMC trajectory is calculated in 200 evenly spaced time increments, using the method detailed in [34]. The dissolved nitrogen concentration in the KMC supercell is held fixed at either $c_{Nm} = 0.1$ at.% or 1.0 at.%, and the vacancy concentration is chosen at discrete points from the range 0.01 at.% $< c_{vm} < 10$ at.%. For each unique combination of c_{vm} and c_{Nm} considered, 48 KMC trajectories consisting of 2.5×10^6 KMC steps are generated at temperatures which are evenly spaced over the range $\frac{1}{227^\circ\text{C}} > \frac{1}{T} > \frac{1}{1538^\circ\text{C}}$. The MSD from the last time increment of each trajectory is used to calculate the diffusion coefficient using equation 7. The diffusion coefficient is also calculated using the MSD from the second-to-last time increment and the MSD after the first half of KMC steps have executed. To ensure that the trajectories are properly converged, it is checked that the logarithm of each of the three calculated diffusion coefficients (in cm^2s^{-1}) differ by no more than 0.05. The KMC supercells are initially populated with nitrogen and vacancies in randomised positions. The first 20% of KMC steps are not included in MSD calculations, to allow time for the nitrogen atoms to approach their equilibrium configurations.

The data generated from the trajectories are used to fit equation 5 using least-squares regression, resulting in a calculated set of a_k^s expressions. If the fitted diffusion coefficient is only dependent on temperature, thus corresponding to a fixed c_{Nm} and c_{vm} pair, the a_k^s are constants. Otherwise, the a_k^s are polynomial expressions of c_N and c_v , each comprising of a set of coefficients which are fitted. Lower-order polynomials are favoured in equation 5 for simplicity and prevention of over-fitting, so all a_k^s where $k > 1$ are set equal to zero unless including higher-order terms would reduce the total squared error by 20% or more. Piecewise log-linear interpolation is used to aid the visualisation of calculated results. For example, suppose that two sets of a_k^s parameters are calculated by fitting equation 5, using a set of KMC trajectories which span the temperature range, at two corresponding vacancy concentrations $c_{v1} = 0.1$ at.% and $c_{v2} = 1$ at.%. Provided the nitrogen concentrations are the same in all the KMC supercells, both fits are only dependent on temperature. Let $D_1^s(T)$ and $D_2^s(T)$ denote the value of the two fits at temperature T . At any temperature, say $T = 500$ K, the logarithm of the diffusion coefficient is calculated for any 0.1 at.% $< c_v < 1$ at.% by the expression $\frac{\log[D_1^s(500)] - \log[D_2^s(500)]}{\log(0.1) - \log(1)} (\log(c_v) - \log(0.1)) + \log[D_1^s(500)]$. The reader is referred to Appendix B for a generalised version of this example.

3. Results and Discussion

3.1. First Principles Results

3.1.1. Ground State Energies

All relevant energy values at the ground state are summarised in table 2. Moreover, the energy barriers for nitrogen to jump between neighbouring octahedral sites are visualised in figure 2a. These values are for constant-volume BCC Fe and FCC Fe, with lattice parameters of 2.838 Å (= 0.2838 nm) and 3.461 Å (= 0.3461 nm) respectively. In vacancy-free BCC Fe the energy barrier was found to be 70.29 kJ mol⁻¹. This value shows fair agreement with other NEB (69.47 kJ mol⁻¹) [8], semi-empirical molecular dynamics (75.26 kJ mol⁻¹) [35] and experimental evaluations (ranging from 70 to 80 kJ mol⁻¹) [10, 36, 37]. In vacancy-free FCC Fe the calculated energy barrier was found to be 218.2 kJ mol⁻¹, but both computational and experimental comparisons are scarce. No documented values were found in literature for comparable NEB calculations using non-magnetic FCC Fe. Semi-empirical molecular dynamics has previously reported a barrier of (131.2 kJ mol⁻¹) [35], which is very far from the NEB value. The most recent experimental evaluation reports a barrier of 167.9 kJ mol⁻¹ [13], which does not show good agreement with either of the two computationally obtained values. However, as detailed in section 3.1.2, taking into account the impact of lattice volume on the DFT-calculated energy barrier results in far closer agreement with the experimental data. Definitive conclusions can not be made about nitrogen diffusion in the presence of vacancies by only considering the $E_{y(i \rightarrow j)}^N$ energy barriers for the individual jumps, and there are no $E_{y(i \rightarrow j)}^N$ values in literature to compare with. However, figure 2a suggests that vacancies form traps for diffusing nitrogen atoms in both phases of iron. This is because the energy barriers for nitrogen to move away from a vacancy $E_{v(i \rightarrow i+1)}^N$ are larger than the reverse jump towards the vacancy $E_{v(i+1 \rightarrow i)}^N$ in all instances.

Table 2: First principles calculation results for interstitial nitrogen and vacancies in ferromagnetic BCC iron and non-magnetic FCC iron. E_{N-N} is the binding energy for nitrogen atom pairs. $E_{v(i)}^N$ is the binding energy for nitrogen atoms which are i 'th nearest neighbours to a vacancy. ΔE^x is the interaction-free energy barrier for x to jump between neighbouring stable positions. $E_{v(i \rightarrow j)}^N$ is the energy barrier for a nitrogen atom to jump from an i 'th to a j 'th nearest neighbour position with respect to a vacancy, and the corresponding energy at the transition site for the jump is denoted $E_{\min(i,j)}^{TS}$. All values are recorded in kJ mol⁻¹. Energy barrier data was reproduced from Karimi and Auinger [3].

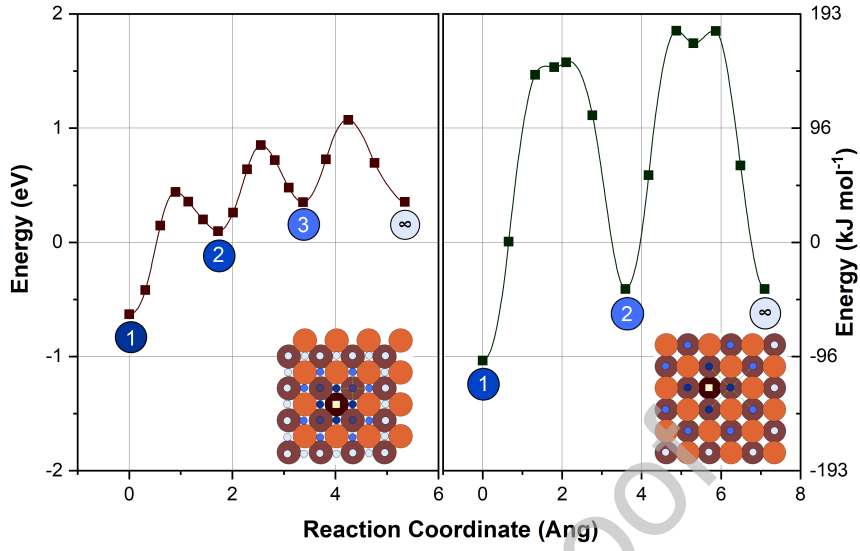
| Lattice | E_{N-N} | $E_{v(1)}^N$ | $E_{v(2)}^N$ | $E_{v(3)}^N$ | $E_{v(\infty)}^N$ | E_1^{TS} | E_2^{TS} | E_∞^{TS} | | |
|---------|-----------|--------------|--------------|--------------|-------------------|----------------------------|----------------------------|----------------------------|----------------------------|--------------|
| BCC | 68.62 | -60.84 | 9.50 | 34.00 | 34.12 | 42.45 | 82.02 | 104.40 | | |
| FCC | 19.04 | -100.01 | -39.45 | - | -39.44 | 152.71 | - | 178.70 | | |
| | | | ΔE^v | | | $E_{v(1 \rightarrow 2)}^N$ | $E_{v(2 \rightarrow 1)}^N$ | $E_{v(2 \rightarrow 3)}^N$ | $E_{v(3 \rightarrow 2)}^N$ | ΔE^N |
| BCC | | | 66.83 | | | 103.29 | 32.95 | 72.52 | 48.02 | 70.29 |
| FCC | | | 139.80 | | | 252.72 | 192.16 | - | - | 218.20 |

Comparing figures 2a and 2b indicates that lone vacancies will migrate at a similar rate to lone nitrogen atoms in BCC Fe, as the calculated ΔE^N and ΔE^v values are within 10 kJ mol⁻¹ of each other. In contrast, it appears that vacancies are substantially more mobile than nitrogen in the FCC lattice as ΔE^v exceeds ΔE^N by almost 100 kJ mol⁻¹.

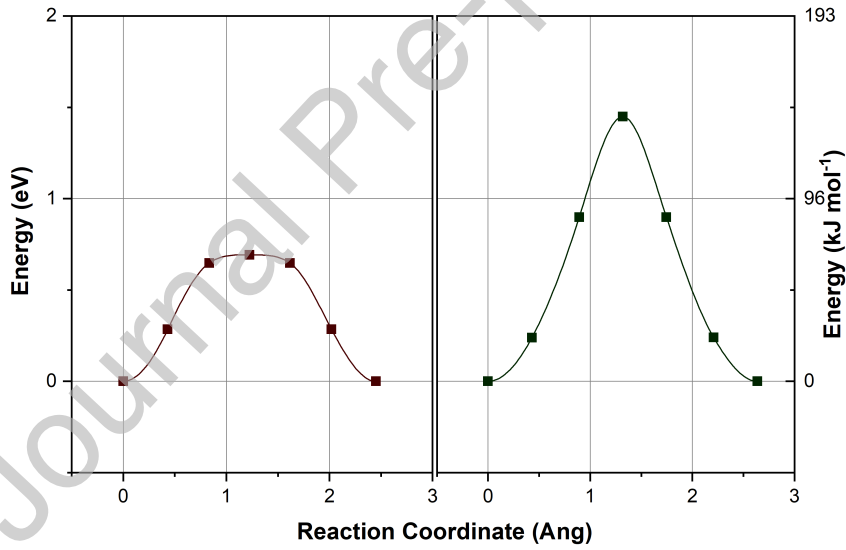
The nearest-neighbour repulsion energies of nitrogen E_{N-N} were found to be 68.62 kJ mol⁻¹ and 19.04 kJ mol⁻¹ for BCC Fe and FCC Fe respectively. Since E_{N-N} was found to be positive for both crystal structures, it prevents the crowding of nitrogen atoms in KMC simulations. Namely, nitrogen atoms will jump to nitrogen-neighbouring octahedral spaces infrequently, due to the contribution of the E_{N-N}^* term in equation 3. The current repulsion model is an approximation which does not account for the effect of a neighbouring nitrogen atom on the transition sites for nitrogen jumps. NEB calculations are needed to refine this by calculating the energy barriers where there is a N-N interaction, such as $E_{N(1 \rightarrow 2)}^N$ and $E_{N(2 \rightarrow 1)}^N$.

3.1.2. Temperature/Volume Dependent Energy Barriers

Figure 3 shows the relationship between the lattice parameter and energy barrier for nitrogen jumps. The data points shown in figure 3 can be fitted to quadratic (for BCC) and linear (for FCC) functions with small residual errors. The dependence of the energy barriers on the thermal expansion of the iron lattice can then be expressed (in kJ mol⁻¹) using the following equations:



(a) Nitrogen migration



(b) Vacancy migration

Figure 2: Results from Nudged Elastic Band (NEB) calculations in BCC (left) and FCC (right) Fe supercells. Each filled square is an NEB data point. **Top:** The energy of an interstitial nitrogen atom in ferromagnetic BCC iron (left) and non-magnetic FCC iron (right) relative to a nitrogen atom in the gas state, as it transitions between octahedral positions (blue shaded circles) in the proximity of a vacancy (filled yellow square in lattice diagrams). The process used to obtain the reference energy of nitrogen gas is detailed in Karimi and Auinger [3]. **Bottom:** The energy of an iron atom in BCC (left) and FCC (right) Fe, as it transitions to a vacant nearest neighbour lattice position.

$$\text{BCC: } E_{v(i \rightarrow j)}^{\text{N}}(V, T) = E_{v(i \rightarrow j)}^{\text{N}}(T) - 0.8613 + 0.006374T - 0.000002056T^2, \quad (8)$$

$$\text{FCC: } E_{v(i \rightarrow j)}^{\text{N}}(V, T) = E_{v(i \rightarrow j)}^{\text{N}}(T) - 36.62 - 0.03854T. \quad (9)$$

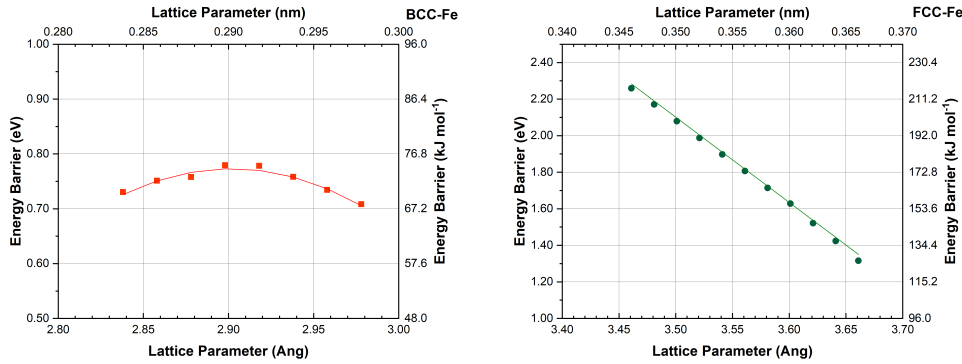


Figure 3: The calculated energy barrier for nitrogen diffusion in α iron (red curve, left) and γ iron (green line, right) when the lattice parameter is varied from its equilibrium value at absolute zero temperature. Filled squares and circles are data points calculated from first principles for ferromagnetic BCC iron and non-magnetic FCC iron respectively.

The first terms in the equations are the energy barriers calculated at the equilibrium lattice parameters determined by DFT, which are temperature dependent at a fixed volume because of vibrational contributions. The vibrational contributions are calculated from the values in table 3 using equation 1. The other terms that follow in equations 8 and 9 represent the volume dependence of the energy barriers as a function of temperature. This is done using well-established linear relationships between the lattice parameters and temperature [32], in combination with the relationships between the lattice parameters and energy barriers calculated in this work (see figure 3). Considering the case where $T = 0$, the volume correction is much larger for FCC Fe. This reflects the larger discrepancy between experimental and DFT-calculated ground state lattice parameters in FCC Fe compared to BCC Fe. The constant terms in equations 8 and 9 scale the DFT-calculated barrier $E_{v(i \rightarrow j)}^N(0)$ to correspond to experimentally-determined lattice parameters (extrapolated to absolute zero temperature), which are -0.7% (BCC Fe) and $+2.8\%$ (FCC Fe) smaller/larger than the lattice parameters used to calculate $E_{v(i \rightarrow j)}^N(0)$. For FCC Fe, volume considerations at absolute zero play a significant role in enforcing agreement between DFT and experimentally calculated nitrogen diffusion data. This is seen through the constant term in equation 9. If $T = 0$ in equation 9, then $\Delta E^N = 181.6 \text{ kJ mol}^{-1}$. This shows more promising agreement with the experimental value of $167.9 \text{ kJ mol}^{-1}$ than the ground state energy barrier of $218.2 \text{ kJ mol}^{-1}$.

Table 3: The zero point energy E_{zpc} , jump attempt frequency ν_N and vibrational energies ϵ_i for a nitrogen interstitial atom in ferromagnetic BCC iron and non-magnetic FCC iron, calculated from first principles. The nitrogen atom is approximated to behave as an independent three-dimensional harmonic oscillator which sits in an octahedral (OCT) or tetrahedral (TS) position in the iron lattice.

| | | Energies (eV) | | | | |
|-----|-------------------------------|---------------|-----------|--------------|--------------|--------------|
| | $\log_{10}(\nu_N \text{ Hz})$ | | E_{zpc} | ϵ_1 | ϵ_2 | ϵ_3 |
| BCC | 12.828 | OCT | 0.095037 | 0.041587 | 0.044928 | 0.103559 |
| | | TS | 0.10105 | 0.035421 | 0.082629 | 0.08405 |
| FCC | 13.052 | OCT | 0.113581 | 0.07468 | 0.075766 | 0.076715 |
| | | TS | 0.108573 | 0.024165 | 0.096123 | 0.096858 |

3.2. Diffusion Model Results

3.2.1. KMC Simulations

Figure 4 shows the calculated diffusion coefficient of nitrogen at each of the 200 time increments for selected KMC trajectories at the start, middle and end of the reciprocal temperature range. In both α Fe and γ Fe, the diffusion coefficient formed by a trajectory generally decreases if the vacancy concentration is increased. The histograms for the trajectories with vacancies also tend to be flatter i.e. less concentrated at the median value. This is because vacancies create large differences in the jump rates by changing the energy barrier in the exponential term of equation 3 in

accordance with table 2. The frequencies of each jump type chosen by the KMC algorithm at each time increment will vary substantially, causing fluctuations in the recorded MSD (see equation 6) values. The effect of the fluctuations with respect to the diffusion coefficient diminish at later time increments as they become smaller with respect to the accumulated MSD. In contrast, the MSD steadily increases at each time increment in the vacancy-free simulations. Hence, the diffusion coefficient converges to its equilibrium value at a much earlier time increment in the vacancy free case.

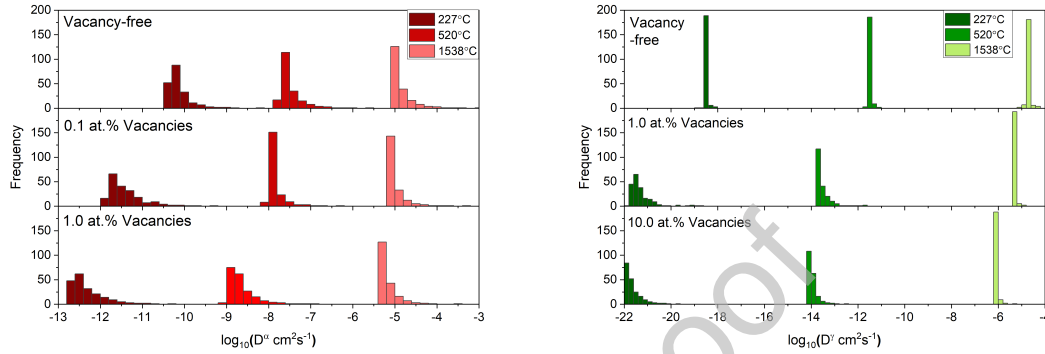


Figure 4: Traces of the diffusion coefficient of interstitial nitrogen atoms from Kinetic Monte Carlo trajectories in ferromagnetic BCC iron (red) and non-magnetic FCC iron (green) supercells. The BCC supercell contained a nitrogen concentration of 0.1 at.%, and the FCC supercell contained a nitrogen concentration of 1 at.%. The supercell for each trajectory had a fixed concentration of vacant lattice positions as labelled.

The trajectory data for each temperature at a chosen vacancy concentration was used to fit the parameters in equation 5, and the residual errors for the fits are recorded in table 4. The corresponding data points for each fit are plotted in Appendix C. The vacancy-free fits have small residual errors regardless of whether the fitting expression is a linear, quadratic or cubic function of reciprocal temperature. Vacancies can cause superlinear growth in the diffusion coefficient as the temperature increases. This is reflected by the larger residual errors in the linear fits for vacancy-rich trajectories in table 4. Increasing the degree of the fitted polynomial, decreases the residual errors. In particular, using a quadratic fit reduces the average residual so it is less than 0.01 in all cases. Over a short temperature range ($< 200^\circ\text{C}$) all fits are approximately linear (see figure C.12 to verify this). Thus, a linear extrapolation is used to extend the lower bound of the temperature range for the fits from 227°C (the smallest KMC temperature) to 100°C so that it can be compared to low-temperature experimental data. Extrapolation is preferred over explicit calculation here, as a lot of computational resources are saved with a negligible effect on the accuracy.

Table 4: The sum of squared residuals (SSR) and average squared residual (ASR) in polynomial fits for the diffusion coefficient of nitrogen in α/γ iron at fixed nitrogen concentration c_N and vacancy concentrations c_V .

| | | Polynomial Fit Degree | | | | | |
|-------------------------------|------------|-----------------------|----------|---------|----------|---------|----------|
| | | 1 | | 2 | | 3 | |
| | c_V at.% | SSR | ASR | SSR | ASR | SSR | ASR |
| α Fe, $c_N = 0.1$ at.% | 0 | 0.02954 | 4.34E-04 | 0.02653 | 3.96E-04 | 0.02408 | 3.65E-04 |
| | 0.1 | 2.78625 | 0.04097 | 0.26359 | 0.00393 | 0.04024 | 6.10E-04 |
| | 1 | 0.67582 | 0.00994 | 0.13175 | 0.00197 | 0.0835 | 0.00127 |
| γ Fe, $c_N = 1$ at.% | 0 | 0.05002 | 7.36E-04 | 0.04933 | 7.36E-04 | 0.04835 | 7.33E-04 |
| | 1 | 1.33366 | 0.01961 | 0.21461 | 0.0032 | 0.13057 | 0.00198 |
| | 10 | 3.35103 | 0.04928 | 0.08166 | 0.00122 | 0.0778 | 0.00118 |

3.2.2. Vacancy-Free Diffusion

Figure 5 shows a comparison between the available experimental data and the calculated vacancy-free diffusion coefficients for nitrogen. The calculated diffusion coefficients are $\log_{10}(D^\alpha(T)) = \frac{-3652}{T} - 3.098$ and $\log_{10}(D^\gamma(T)) = \frac{-9515}{T} + 0.4588$. The most significant discrepancies between the experimental and calculated sources are seen for the BCC Fe phases (α and δ) at higher temperatures. This is because a single linear Arrhenius-type fit can not accurately portray nitrogen diffusion in BCC iron up to its melting point [10]. Diffusion-enhancing magnetic effects [36] are thought to be the cause of divergence from a single linear fit in the experimental data, which are not incorporated in the computational model. As documented by [10], the experimental data can be separated into two linear fits at the point where $\frac{1}{T} = 0.0029$. The low-temperature fit ($\frac{1}{T} > 0.0029$) of $\log_{10}(D^\alpha(T)) = \frac{-3727}{T} - 3.376$ is outside of the temperature range calculated in this work. However, because the data is linear, the calculated fit should extrapolate accurately to lower temperatures. Indeed, comparing the energy barriers (-3727 and -3652) and prefactors (-3.376 and -3.098) shows agreement between the low-temperature experimental fit and the calculated fit for α Fe. In contrast, the high-temperature fit ($\frac{1}{T} < 0.0029$) of $\log_{10}(D^\alpha(T)) = \frac{-4176}{T} - 2.001$ shows divergence from the low-temperature fits.

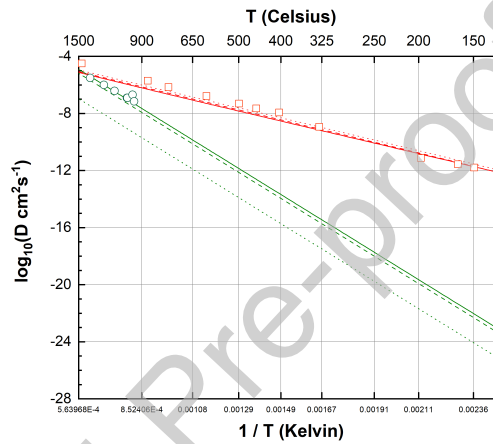


Figure 5: Nitrogen diffusion data calculated from first principles in ferromagnetic BCC iron (red lines) and non-magnetic FCC iron (green lines). Solid lines indicate that volume and vibrational contributions are incorporated into the calculation. Dashed lines indicate only volume contributions are included, while the dotted lines indicate both contributions are omitted. Experimental diffusion data for α iron [10] (red squares) and γ iron [13] (green circles) are included for comparison.

In nitrogen-saturated iron, an experimentally-calculated diffusion coefficient will deviate from the values in figure 5. The KMC supercells are assumed to retain a cubic crystal structure under all diffusion conditions considered in this work. However, in BCC Fe nitrogen interstitials induce a local tetrahedral distortion. If the nitrogen concentration is small enough that the nitrogen atoms rarely interact, the distortion does not impact diffusion. However, due to the distortion, neighbouring nitrogen interstitials will have asymmetric diffusion pathways. When the nitrogen concentration is high, the energies of the octahedral stable sites and tetrahedral transition sites will not be equivalent throughout the lattice. This effect makes the energy barrier for nitrogen diffusion dependant on the nitrogen concentration. The experimentally calculated diffusion coefficient of nitrogen does not deviate significantly in dilute nitrogen concentrations up to at least $c_N = 0.7$ at.% [38]. Looking to the analogous case of carbon interstitials, which are more studied than nitrogen interstitials in this regard, the impact on diffusion is significant at a solute concentration of 5 at.% where the energy barrier differs by around 10 kJ mol^{-1} compared to the dilute case [39]. Similar effects would likely be observed for nitrogen interstitials, as the divergence from a cubic crystal in super-saturated Fe-N is significant at $c_N = 4.4$ at.% [40]. Furthermore, Fe_{16}N_2 forms in Fe-N martensites at low temperatures ($< 400 \text{ K}$) [41]. This affects the diffusivity of nitrogen in a substantial concentration range ($0.05 \text{ at.}\% < c_N < 11 \text{ at.}\%$). More information is needed to assess the extent of these effects if vacancies are introduced, as vacancies significantly change the conditions where each type of nitride is stable [3].

The nitrogen concentration dependency found experimentally in austenite (FCC Fe) is particularly strong when the nitrogen concentration exceeds 1 at.% [11], and the underlying reasoning for this may not be incorporated in the

current model. For instance, the findings of this work suggest that volume-considerations are important (see figure 5) for nitrogen diffusion in austenite. The model considers the thermal expansion of the Fe lattice, but it does not consider the substantial lattice expansion which is induced by increasing the nitrogen concentration [42].

3.2.3. Impact of Vacancies

The presence of vacancies in excess of their expected concentration at thermal equilibrium can result in significantly slower nitrogen diffusion in both α and γ Fe. At fixed nitrogen concentration, the diffusion coefficient decreases with increased vacancy concentration. The impact of vacancies on diffusion is less pronounced at higher temperatures because nitrogen atoms are more likely to escape from them. This can be seen by considering the definition of a jump rate in equation 3. As the temperature increases, all jump rates approach a common value of ν_x , meaning that the random walk followed by nitrogen atoms approaches a symmetrical random walk. Hence, the dynamics simulation closely resembles interaction-free (between nitrogen and vacancies) diffusion at high temperatures.

There are 42 and 38 octahedral trapping sites around a vacancy in BCC and FCC crystals respectively, with 48 and 78 transition events between trapping sites to the interaction-free sites. Therefore, α Fe has more sites to hold nitrogen atoms, and there are fewer routes for those trapped atoms to escape. However, there are three octahedral spaces for each lattice space in a BCC crystal, meaning that it has a larger proportion of interaction-free sites relative to a FCC crystal with the same vacancy concentration. Migration to vacancies in α Fe was generally calculated to be more energetically favoured than in γ Fe. For instance, $E_{v(1\rightarrow2)}^N - E_{v(2\rightarrow1)}^N = 70.3 \text{ kJ mol}^{-1}$ and 60.6 kJ mol^{-1} for α and γ respectively. The repulsion energy between two nitrogen atoms in α was found to be much larger (see section 3.1.1). A higher repulsion energy reduces the ability of vacancies to trap multiple nitrogen atoms, meaning that the trapping effect diminishes quickly if the nitrogen concentration is higher than the vacancy concentration.

Figure 6 quantifies the decrease in the nitrogen diffusion coefficient when the vacancy concentration increases. The nitrogen concentrations are fixed at $c_N = 0.1 \text{ at.}\%$ for α Fe and $c_N = 1 \text{ at.}\%$ for γ Fe, which are chosen to represent typical nitrogen solubility values for each phase. The dashed black curves highlight where $c_v = c_N$, which signifies an important change in the dynamics of the KMC simulations because each nitrogen has at least one vacancy to bind to. At low temperatures, the binding is so strong that the nitrogen atoms are barely mobile enough to explore the supercell, so increasing the concentration of vacancies has a limited impact on the already 'frozen' nitrogen. As the temperatures increase, increasing the vacancy concentration has a more pronounced effect on diffusion. This effect can be seen from the $c_v = c_N$ curves in figure 6, because they increase at a superlinear rate as the temperature increases. In α Fe the curve is close to vacancy-free diffusion at high temperatures, but it diverges at low temperatures where the trapping effect is stronger. In γ Fe, the curve is close to the lower bound of diffusion speed in the vacancy range tested i.e. the fitted curves with $c_v = 1 \text{ at.}\%$ and $c_v = 10 \text{ at.}\%$ are similar. Thus, there is a large difference in the behaviour of α Fe with $c_N = 0.1 \text{ at.}\%$ and γ Fe with $c_N = 1 \text{ at.}\%$ when $c_v > c_N$. This can also be seen in figure 7; in the γ case there is a sharp change at $c_v = c_N = 1 \text{ at.}\%$ where increasing the vacancy concentration has minimal impact on diffusion; in α the diffusion speed consistently decreases when the vacancy concentration increases. A significant consideration here is that in α Fe the concentrations are an order of magnitude smaller than in γ Fe, meaning that interactions are overall less likely. When $c_v = c_N = 0.1 \text{ at.}\%$ there is a vacancy available to pair with each nitrogen, but the nitrogen-vacancy encounter rate is lower than for $c_v = c_N = 1 \text{ at.}\%$. Indeed, the diffusion coefficient for $c_v = c_N = 0.1 \text{ at.}\%$ in γ Fe was found to closely correspond to vacancy-free diffusion, which contrasts the $c_v = c_N = 1 \text{ at.}\%$ case which is depicted in figure 6.

The vacancy concentrations which are investigated ($0.01 \text{ at.}\% < c_v < 10 \text{ at.}\%$) represent extreme levels of deformation which do not necessarily arise under common manufacturing conditions. However, it can be seen from figure 7 that the impact of vacancies is greatly diminished if the vacancy concentration is an order of magnitude smaller than the nitrogen concentration. This suggests that extreme levels of deformation are required in order to observe significant disruption of nitrogen diffusion due to vacancy-related effects. It has previously been shown in the case of nitrogen solubility that vacancy-rich models from first principles can depict the nature of nitrogen in iron more accurately than vacancy-free models [3]. There is evidence that the same applies for the diffusion model in this work, although a conclusive judgement is not possible with the experimental data that is currently available. Concerning low-temperature diffusion data for α Fe, the Arrhenius fit for the experimental data is close to the calculated fit, but it is strictly smaller over the temperature range with a steeper gradient and a smaller prefactor (see section 3.2.2). Moreover, the low-temperature experimental data points ($< 200^\circ\text{C}$) in figure 6 are all below the calculated vacancy-free diffusion fit. The diffusion data measured by low-temperature experiments is better represented by the calculated data

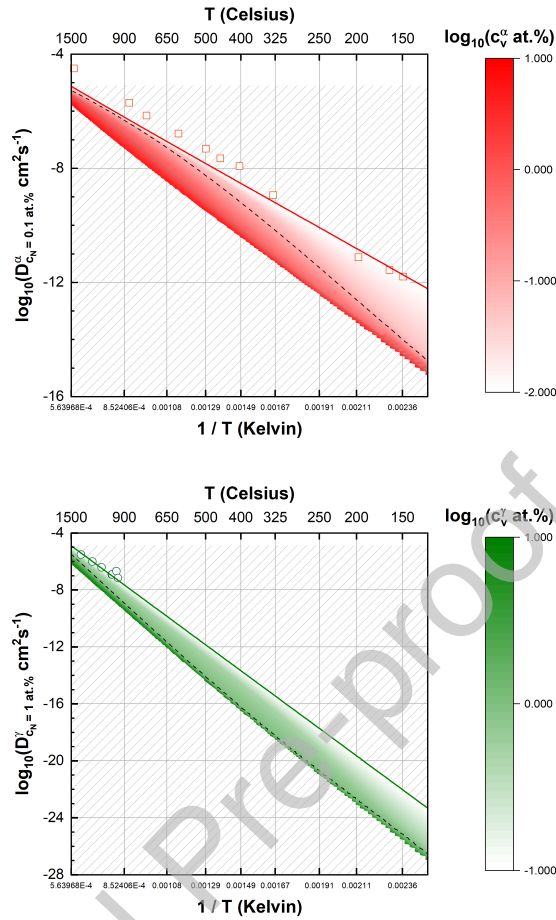


Figure 6: The interstitial diffusion coefficient D of nitrogen in α iron (red, top) and γ iron (green, bottom) calculated with nitrogen concentrations $c_N = 0.1$ at.% and $c_N = 1.0$ at.% respectively. Experimental data points for comparison are from [10] (red squares) and [13] (green circles). The diffusion coefficients calculated in absence of vacancies are given by red and green solid lines. The contour surfaces indicate the shift in diffusion coefficient at varied vacancy concentrations. The dashed black curves on the contour surfaces indicate where the nitrogen and vacancy concentrations are equal.

with vacancy concentrations of around $0.01 \text{ at.}\% < c_v < 0.1 \text{ at.}\%$, which is many orders of a magnitude higher than the vacancy concentration expected at equilibrium. It is not possible to conclude if the situation is similar for high-temperature α Fe, as there are deviations which are thought to be unrelated to vacancies (discussed in section 3.2.2), and the effect of vacancies are smaller at higher temperatures. All of the experimental data points for γ Fe are above 912°C , because high-purity γ Fe is not stable at lower temperatures. Therefore, as seen in figure 6, a vacancy concentration larger than $0.1 \text{ at.}\%$ would be required to disrupt nitrogen diffusion to a significant extent. This is unlikely in experiments which intentionally use pure and well-formed Fe, so it is not surprising that the experimental data is in close agreement with the vacancy-free calculation.

The current model is limited to singular point defect interactions. However, when nitrogen and vacancies are abundant within iron, larger nitrogen-vacancy complexes can form [3, 16, 43]. This may result in deviations between the calculated and experimental diffusion data, particularly when the concentrations of nitrogen or vacancies exceed that of the DFT supercells which were used to calculate the energy barriers (see table 1). From the size of the DFT supercells, the concentrations where such deviations could begin to occur are estimated to be around $1.9 \text{ at.}\%$ and $2.1 \text{ at.}\%$ for α and γ Fe respectively. Concerning mono-vacancy multi-nitrogen complexes, the deviations should not be significant. In both α and γ Fe the most abundant complexes of this type are those containing one (vN) or two

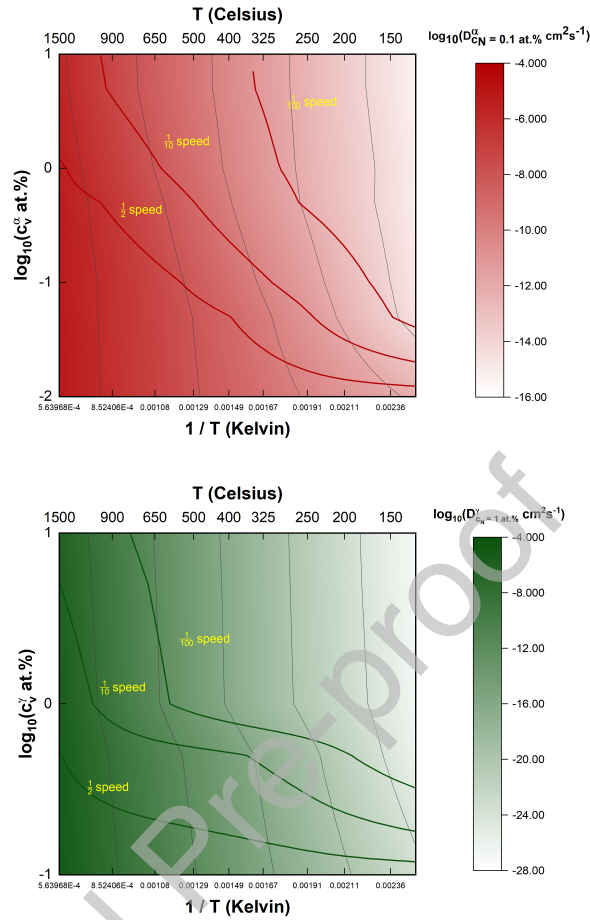


Figure 7: The contour surface which portrays the shift in the diffusion coefficient of nitrogen in α iron (red, top) and γ iron (green, bottom) at varied vacancy concentrations and temperatures. The nitrogen concentration is fixed at 0.1 at.% and 1 at.% for α and γ respectively. red and green lines on the surfaces trace the points where the diffusion coefficient has decreased (compared to vacancy-free diffusion) 2, 10 and 100-fold due to vacancies.

(vN_2) nitrogen atoms. The respective difference in nitrogen binding energies between vN and vN_2 for either Fe phase does not exceed 10 kJ mol^{-1} [3]. Therefore, the jump rates associated with the vN complex are a good approximation for the rates associated with the vN_2 complex, while complexes with three or more nitrogen atoms are rare enough to disregard for most applications. Insufficient information is available to deduce the significance of multi-vacancy multi-nitrogen complexes, meaning that the calculated results should be treated with scrutiny when $1 \text{ at.}\% < c_v < 10 \text{ at.}\%$ as the omitted vacancy-vacancy interactions would be frequent. Furthermore, the nitrogen repulsion energy used in the calculations is not affected by the presence of vacancies. Hence, the current repulsion model does not capture the nuances of nitrogen-vacancy interactions. However, it has the desirable effect of discouraging the formation of overly nitrogen-dense complexes which are non-physical.

3.2.4. Vacancy-Dependent Diffusion Coefficient

In order to cast the calculated diffusion data in an applied setting, it is used to fit diffusion coefficients as functions of nitrogen concentration, vacancy concentration and temperature. In particular, each a_k^s from equation 5 is expressed as a function of c_v and c_N . Two intuitive considerations are used to choose the form of the a_k^s . Firstly, the vacancy mixing ratio $\frac{c_v}{c_v + c_N}$ is closely tied to the trapping ability of vacancies. If there are few vacancies relative to nitrogen atoms, then the vacancy contribution to the diffusivity of nitrogen will be small, as the displacement is averaged over

all nitrogen atoms (see equation 6). However, the mixing ratio is not sufficient to fully capture the relationship. If the absolute vacancy concentration is small, nitrogen-vacancy interactions will be unlikely regardless of what the mixing ratio is. To account for both the ratio and the absolute vacancy concentration, each parameter of equation 5 is expressed as $a_k^s = \sum_j b_j \log_{10} \left(\frac{c_v^2}{100(c_v+c_N)} \right)^j$ where the b_j are obtained from least squares fitting. The reader is referred to table 5 for the fitted parameter values and the spreadsheet in the supplementary data for example usages.

In this work, the parameters are only calculated at nitrogen concentrations of 0.1 at.% and 1.0 at.%, meaning that they will not generalise over a range of nitrogen concentrations as well as they do in a range of vacancy concentrations. The fit corresponding to $c_N = 1$ at.% in α Fe is used to validate the $c_N = 0.1$ at.% fit, and similarly the $c_N = 1$ at.% fit is validated against the $c_N = 0.1$ at.% fit in γ Fe. This approximates the upper bounds of error from generalising the diffusion coefficient to varied nitrogen concentrations over the full range of conditions as shown in figure 8.

Table 5: Fitted parameters for diffusion coefficients of nitrogen in α iron and γ iron which are dependent on nitrogen concentration c_N , vacancy concentration c_v and temperature T Kelvin. The fits are valid in a range of $\log_{10} \left(\frac{c_v^2}{100(c_v+c_N)} \right)$ values which are specified in the table. AR denotes the average residual error of the fit.

| | | | | | | |
|-------------------------------|-----------|--|--|-----------|-----------|-----------|
| α Fe, $c_N = 0.1$ at.% | | $\log_{10} \left(\frac{c_v^2}{100(c_v+c_N)} \right)_{\min}$ | $\log_{10} \left(\frac{c_v^2}{100(c_v+c_N)} \right)_{\max}$ | AR (%) | | |
| | | -5.04E+00 | -1.01E+00 | 4.48E-01 | | |
| | | b_0 | b_1 | b_2 | b_3 | b_4 |
| | a_0 | -4.80E+00 | -2.35E+00 | -3.41E-01 | 1.84E-01 | 3.44E-02 |
| | a_1 | -9.19E+02 | 7.07E+03 | 3.08E+03 | 3.15E+02 | -8.03E+00 |
| a_2 | -1.37E+06 | -2.54E+06 | -1.21E+06 | -1.56E+05 | -9.87E+02 | |
| α Fe, $c_N = 1$ at.% | | $\log_{10} \left(\frac{c_v^2}{100(c_v+c_N)} \right)_{\min}$ | $\log_{10} \left(\frac{c_v^2}{100(c_v+c_N)} \right)_{\max}$ | AR (%) | | |
| | | -6.00E+00 | -1.04E+00 | 5.88E-01 | | |
| | | b_0 | b_1 | b_2 | b_3 | b_4 |
| | a_0 | -4.84E+00 | -3.21E+00 | -1.62E+00 | -3.17E-01 | -2.14E-02 |
| | a_1 | -3.22E+03 | 4.03E+03 | 2.57E+03 | 5.55E+02 | 3.95E+01 |
| a_2 | 3.80E+05 | 3.57E+05 | 1.63E+05 | 3.29E+04 | 2.35E+03 | |
| γ Fe, $c_N = 0.1$ at.% | | $\log_{10} \left(\frac{c_v^2}{100(c_v+c_N)} \right)_{\min}$ | $\log_{10} \left(\frac{c_v^2}{100(c_v+c_N)} \right)_{\max}$ | AR (%) | | |
| | | -5.04E+00 | -1.00E+00 | 1.06E+00 | | |
| | | b_0 | b_1 | b_2 | b_3 | |
| | a_0 | -3.87E+00 | -6.31E+00 | -2.30E+00 | -2.42E-01 | |
| | a_1 | -5.62E+03 | 9.89E+03 | 4.10E+03 | 4.56E+02 | |
| a_2 | -4.54E+05 | -1.36E+06 | -5.88E+05 | -6.69E+04 | | |
| γ Fe, $c_N = 1$ at.% | | $\log_{10} \left(\frac{c_v^2}{100(c_v+c_N)} \right)_{\min}$ | $\log_{10} \left(\frac{c_v^2}{100(c_v+c_N)} \right)_{\max}$ | AR (%) | | |
| | | -4.04E+00 | -1.04E+00 | 9.69E-01 | | |
| | | b_0 | b_1 | b_2 | b_3 | |
| | a_0 | -1.06E+01 | -1.69E+01 | -7.22E+00 | -9.18E-01 | |
| | a_1 | 8.67E+03 | 3.23E+04 | 1.44E+04 | 1.86E+03 | |
| a_2 | -6.13E+06 | -1.03E+07 | -4.65E+06 | -6.12E+05 | | |

It is reported in literature that carbon interstitials, like nitrogen interstitials, are strongly attracted to vacancies [16]. Therefore, carbon atoms could compete with nitrogen for energetically favourable locations around vacancies, acting as a deterrent to nitrogen trapping near vacancies. This would suggest that the quantified results are lower bounds of an experimentally-calculated diffusion coefficient, because they carry the underlying assumption that the available trapping sites are solely accessible to nitrogen. This would be a particularly important consideration when the carbon concentration exceeds the nitrogen concentration. Moreover, the calculated diffusion coefficient in this work is dependent on nitrogen concentration, but it is invariant under changing nitrogen concentration unless the vacancy concentration is greater than zero. This is a simplification. As discussed in section 3.2.2, the diffusion coefficient is

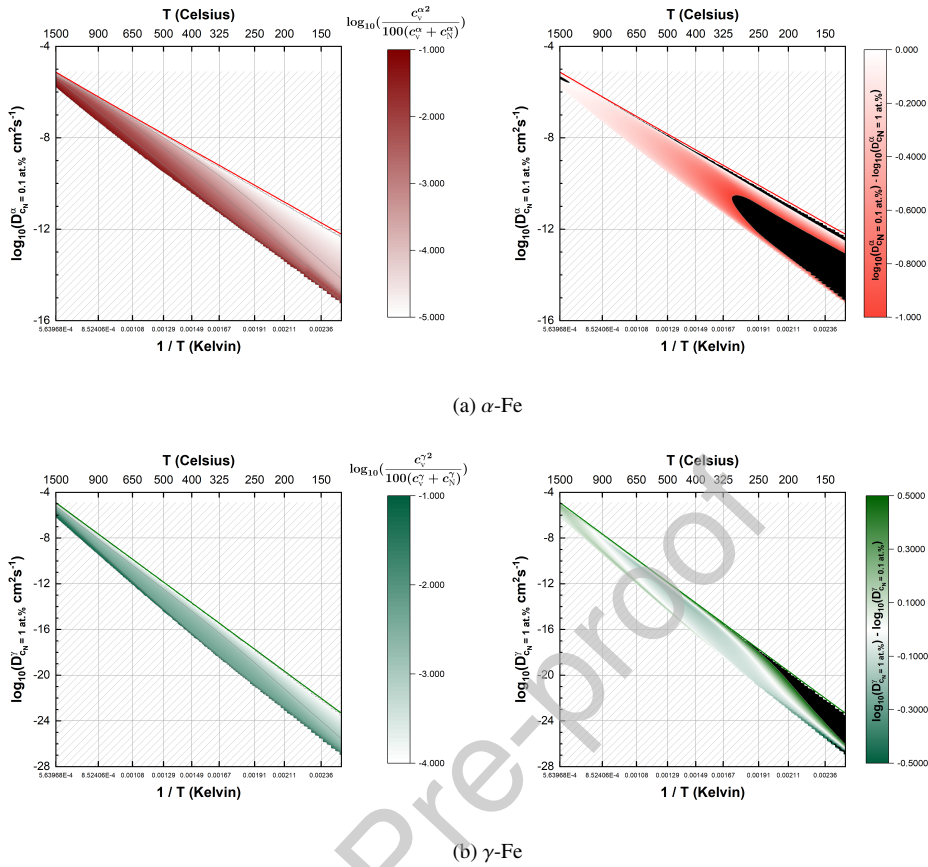


Figure 8: The diffusion coefficient of nitrogen in vacancy-containing α iron (red, top) and γ iron (green, bottom). The figures on the left hand side indicate the shift in the diffusion coefficient at a range of values of the expression $\log_{10}\left(\frac{c_v^2}{100(c_v + c_N)}\right)$, where c_N is the nitrogen concentration and c_v is the vacancy concentration. The left hand side figures are calculated with interstitial nitrogen concentrations of $c_N = 0.1$ at.% and $c_N = 1$ at.% for α iron and γ iron respectively. The figures on the right hand side shows the difference between polynomial fits of the diffusion coefficient corresponding to two different nitrogen concentrations. The areas where the difference between the fits is outside of the colour bar range of the contours is coloured in black.

dependent on the nitrogen concentration in vacancy-free Fe.

3.3. Using the Supplementary Spreadsheet

3.3.1. Vacancy-Free Diffusion

In the vacancy-free case there is only one input to the spreadsheet, which is the temperature in $^{\circ}\text{C}$. This should be entered into cell A6. Cell E7 will turn red to warn the user if the input temperature is outside of the validity range of the fit. The corresponding diffusion coefficient for nitrogen is calculated in U10 and U19 for α Fe and γ Fe respectively.

3.3.2. Vacancy-Dependent Diffusion

In the vacancy-dependent case there are three inputs to the spreadsheet, the nitrogen concentration, vacancy concentration and temperature. The temperature input is the same as in section 3.3.1. The nitrogen concentration and vacancy concentration are entered into cells A31 and B31, respectively. There are four diffusion coefficients calculated in total, which are found in cells U36 (α Fe, $c_N = 0.1$ at.%), U50 (α Fe, $c_N = 1$ at.%), U71 (γ Fe, $c_N = 0.1$ at.%) and U85 (γ Fe, $c_N = 1$ at.%). Each of the diffusion coefficients is calculated using the fitted parameters recorded in table 5. Potential issues with the calculated diffusion coefficient at the chosen conditions are flagged by the diagnostic

cells: U62, V36, and V50 for α Fe; U97, V71 and V85 for γ Fe. The examples that follow show how to interpret the calculated result and use the diagnostic cells for α Fe, and similar statements apply to γ Fe.

Example 1.

- Input $T = 500^\circ\text{C}$, $c_v = 0.5$ at.% and $c_N = 0.1$ at.%.
- The value of U50 should be disregarded, as an experimentally-calculated diffusion coefficient will closely match U36. This is because the parameters which are used to calculate U36 are fitted from simulation data where $c_N = 0.1$ at.%.

Example 2:

- Input $T = 500^\circ\text{C}$ and $c_v = c_N = 0.5$ at.%.
- An experimentally-calculated diffusion coefficient should be in the interval between U36 and U50. However, because $c_N = 0.5$ at.% is close to $c_N = 1$ at.% on a logarithmic scale, the diffusion coefficient is likely much closer to U50 than U36.
- The maximum error caused by using interpolation to calculate the diffusion coefficient for 0.1 at.% $< c_N < 1$ at.% is displayed in U62, which is the length of the interval between U36 and U50. However, this is the absolute upper bound. If the two calculated diffusion coefficients are weighted appropriately, the error is likely to be smaller. Moreover, as shown in figure 8a the error varies greatly with temperature. At some temperatures the nitrogen concentration can be changed without significantly increasing the margin for error.

Example 3:

- Input $T = 500^\circ\text{C}$, $c_v = 0.001$ at.% and $c_N = 0.1$ at.%.
- At the chosen nitrogen concentration one might expect that the diffusion coefficient in U36 closely resembles an experimentally-calculated diffusion coefficient. However, in this case V36 is highlighted in red. This is to indicate that the U36 value exceeds the vacancy-free diffusion coefficient for α Fe, so it is no longer in the coloured region of figure 8a (left hand side) at the chosen temperature. This can be verified by cross-referencing the figure with the value in cell E31.
- The vacancy concentration is much smaller than the nitrogen concentration. This means that the value of $\log_{10}\left(\frac{c_v^2}{100(c_v+c_N)}\right)$ is below the minimum threshold for the fit to be valid. However, the vacancy-free diffusion coefficient (U10) closely resembles an experimentally-calculated diffusion coefficient, because the vacancy contribution to diffusion will be accordingly small.

4. Conclusion

A robust multi-scale model was used in this work to generate nitrogen diffusion data in iron from first principles. The data was used to fit polynomial expressions so that it can be incorporated in applied settings, such as layer growth models for nitriding or further experimental research. Nitrogen diffusion was systematically investigated in α and γ Fe to enhance the clarity of the current literature. In particular, it is shown that non-magnetic FCC Fe can be a suitable candidate to model γ Fe for this purpose, provided that thermal expansion considerations are included. Good agreement was found between the diffusion model used in this work and the available experimental nitrogen diffusion data for both phases of iron. The model quantifies the effect of vacancies, and it was found that both the vacancy concentration and the nitrogen-vacancy ratio can have a large impact on the diffusion speed of nitrogen. A direct method to quantify this impact is provided through the diffusion coefficients of nitrogen in each phase, which are valid in a range of temperatures ($100^\circ\text{C} < T < 1538^\circ\text{C}$), nitrogen concentrations (0.1 at.% $< c_N < 1$ at.% with potential to extrapolate), and vacancy concentrations (0.01 at.% $< c_v < 10$ at.%). For the considered conditions, it appears that significant deformation ($c_v > 0.01$ at.%) is required to disrupt nitrogen diffusion to an extent which is experimentally observable. The predicted upper limit of errors under the conditions examined (see figure 8) shows that in most cases, the diffusion coefficients calculated in this work yield an enhanced method for determining nitrogen diffusibility in vacancy-rich iron.

5. Acknowledgements

The authors thank the Centre for Scientific Computing (CSC, University of Warwick) for their support and providing computation time on their high performance computing cluster.

6. References

References

- [1] Y. Deng, C. Tan, Y. Wang, L. Chen, P. Cai, T. Kuang, S. Lei, and K. Zhou. Effects of tailored nitriding layers on comprehensive properties of duplex plasma-treated alitin coatings. *Ceramics International*, 43, 04 2017.
- [2] O. Kessler, F. Hoffmann, and P. Mayr. The role of cvd parameters in producing the eggshell effect during the coating of steel. *Chemical Vapor Deposition*, 6(5):253–259, 2000.
- [3] A. Karimi and M. Auinger. Thermodynamics of the iron-nitrogen system with vacancies. from first principles to applications. *Journal of Alloys and Compounds*, 821:153343, 2020.
- [4] K. Dawi, C.-W. He, M.-F. Barthe, P. Desgardin, and A. Volgin. Vacancy defects study in fe based alloys induced by irradiation under various conditions. *Journal of Physics: Conference Series*, 505:012007, 2014.
- [5] N. Igata, R. Hasiguti, and S. Seto. Behaviors of nitrogen atoms in irradiated iron and iron alloy revealed by internal friction and electron microscopy. *Trans. Iron Steel Inst. Jap.*, 10:21–24, 1970.
- [6] T.R Anthony. Solute segregation in vacancy gradients generated by sintering and temperature changes. *Acta Metallurgica*, 17(5):603–609, 1969. ISSN 0001-6160.
- [7] A. Garipy, H. Miao, and M. Lvesque. 3.12 - peen forming. In Saleem Hashmi, Gilmar Ferreira Batalha, Chester J. Van Tyne, and Bekir Yilbas, editors, *Comprehensive Materials Processing*, pages 295 – 329. Elsevier, Oxford, 2014.
- [8] M.H. Wu, X.H. Liu, J.F. Gu, and Z.H. Jin. First-principles simulations of iron with nitrogen: from surface adsorption to bulk diffusion. *Modelling and Simulation in Materials Science and Engineering*, 21(4):045004, 2013.
- [9] S. Sakuraya, K. Takahashi, N. Hashimoto, and S. Ohnuki. The effect of point defects on diffusion pathway within α -fe. *Journal of Physics Condensed Matter*, 27(17):175007, 2015.
- [10] M.L. Wasz and R.B. McLellan. Nitrogen diffusion in bcc iron. *Scripta Metallurgica et Materialia*, 28:1461–1463, 1993.
- [11] S. Mändl and B. Rauschenbach. Concentration dependent nitrogen diffusion coefficient in expanded austenite formed by ion implantation. *Journal of Applied Physics*, 91(12):9737–9742, 2002.
- [12] J.T. Slycke, E.J. Mittemeijer, and M.A.J. Somers. 1 - thermodynamics and kinetics of gas and gassolid reactions. In *Thermochemical Surface Engineering of Steels*, pages 3–111. Woodhead Publishing, Oxford, 2015.
- [13] P. Grieveson and E.T. Turkdogan. Iron and steel division - kinetics of reaction of gaseous nitrogen with iron part i: Kinetics of nitrogen solution in gamma iron. *The American Institute of Mining, Metallurgical, and Petroleum Engineers*, 230:1604, 1964.
- [14] M.H. Wu, X.H. Liu, J.F. Gu, and Z.H. Jin. Dft study of nitrogen-vacancy complexions in (fcc) fe. *Modelling and Simulation in Materials Science and Engineering*, 22(5):055004, 2014.
- [15] D. Jiang and E.A. Carter. Carbon dissolution and diffusion in ferrite and austenite from first principles. *Phys. Rev. B*, 67:214103, 2003.
- [16] C. Barouh, T. Schuler, C.C. Fu, and T. Jourdan. Predicting vacancy-mediated diffusion of interstitial solutes in α -fe. *Phys. Rev. B*, 92:104102, 2015.
- [17] A.L. Nikolaev and T.E. Kurenykh. On the interaction between radiation-induced defects and foreign interstitial atoms in -iron. *Journal of Nuclear Materials*, 414(3):374–381, 2011.
- [18] F. Walz, H. J. Blythe, and H. Kronmiller. Binding enthalpies of nitrogen-vacancy complexes in irradiated α -fe. *Radiation Effects and Defects in Solids*, 116(4):339–352, 1991.
- [19] T. Schuler and M. Nastar. Transport properties of dilute α -Fe(x) solid solutions ($x = C, N, O$). *Phys. Rev. B*, 93:224101, Jun 2016.
- [20] J.J. Mortensen, L.B. Hansen, and K.W. Jacobsen. Real-space grid implementation of the projector augmented wave method. *Phys. Rev. B*, 71:035109, 2005.
- [21] J. Enkovaara, C. Rostgaard, J.J. Mortensen, J. Chen, M. Duřak, L. Ferrighi, J. Gavnholt, C. Glinsvad, V. Haikola, H.A. Hansen, H.H. Kristoffersen, M. Kuusma, A.H. Larsen, L. Lehtovaara, M.L. Jungberg, O. Lopez-Acevedo, P.G. Moses, J. Ojanen, T. Olsen, V. Petzold, N.A. Romero, J. Stausholm-Müller, M. Strange, G.A. Tritsarlis, M. Vanin, M. Walter, B. Hammer, H. Häkkinen, G.K.H. Madsen, R.M. Nieminen, J.K. Nørskov, M. Puska, T.T. Rantala, J. Schiøtz, K.S. Thygesen, and K.W. Jacobsen. Electronic structure calculations with gpaw: a real-space implementation of the projector augmented-wave method. *Journal of Physics: Condensed Matter*, 22(25):253202, 2010.
- [22] J.P. Perdew, K. Burke, and M. Ernzerhof. Generalized gradient approximation made simple. *Phys. Rev. Lett.*, 77:3865–3868, 1996.
- [23] A.H. Larsen, J.J. Mortensen, J. Blomqvist, I.E. Castelli, R. Christensen, M. Duřak, J. Friis, M.N. Groves, B. Hammer, C. Hargus, E.D. Hermes, P.C. Jennings, P.B. Jensen, J. Kermode, J.R. Kitchin, E.L. Kolsbjerg, J. Kubal, K. Kaasbjerg, S. Lysgaard, J.B. Maronsson, T. Maxson, T. Olsen, L. Pastewka, A. Peterson, C. Rostgaard, J. Schiøtz, O. Schütt, M. Strange, K.S. Thygesen, T. Vegge, L. Vilhelmsen, M. Walter, Z. Zeng, and K.W. Jacobsen. The atomic simulation environmenta python library for working with atoms. *Journal of Physics: Condensed Matter*, 29(27):273002, 2017.
- [24] H.J. Monkhorst and J.D. Pack. Special points for brillouin-zone integrations. *Phys. Rev. B*, 13:5188–5192, 1976.
- [25] M. Methfessel and A.T. Paxton. High-precision sampling for brillouin-zone integration in metals. *Phys. Rev. B*, 40:3616–3621, 1989.
- [26] H. Jónsson, G. Mills, and K.W. Jacobsen. *Classical and Quantum Dynamics in Condensed Phase Simulations*, chapter 16 - Nudged elastic band method for finding minimum energy paths of transitions, pages 385–404. World Scientific, 1998.
- [27] G. Henkelman, B.P. Uberuaga, and H. Jónsson. A climbing image nudged elastic band method for finding saddle points and minimum energy paths. *The Journal of Chemical Physics*, 113(22):9901–9904, 2000.

- [28] E. Bitzek, P. Koskinen, F. Gähler, M. Moseler, and P. Gumbsch. Structural relaxation made simple. *Phys. Rev. Lett.*, 97:170201, 2006.
- [29] Keyvan Ferasat, Yuri N. Osetsky, Alexander V. Barashev, Yanwen Zhang, and Zhongwen Yao. Accelerated kinetic monte carlo: A case study; vacancy and dumbbell interstitial diffusion traps in concentrated solid solution alloys. *The Journal of Chemical Physics*, 153(7):074109, 2020.
- [30] Brian Puchala, Michael L. Falk, and Krishna Garikipati. An energy basin finding algorithm for kinetic monte carlo acceleration. *The Journal of Chemical Physics*, 132(13):134104, 2010.
- [31] Craig Daniels and Pascal Bellon. Hybrid kinetic monte carlo algorithm for strongly trapping alloy systems. *Computational Materials Science*, 173:109386, 2020.
- [32] Z.S. Basinski, W. Hume-Rothery, and A.L. Sutton. The lattice expansion of iron. *Proceedings of the Royal Society of London. Series A, Mathematical and Physical Sciences*, 229(1179):459–467, 1955.
- [33] M. Leetmaa and N.V. Skorodumova. KmcLib: A general framework for lattice kinetic monte carlo (kmc) simulations. *Computer Physics Communications*, 185(9):2340 – 2349, 2014.
- [34] M. Leetmaa and N.V. Skorodumova. Mean square displacements with error estimates from non-equidistant time-step kinetic monte carlo simulations. *Computer Physics Communications*, 191:119–124, 2015.
- [35] B.J. Lee, T.H. Lee, and S.J. Kim. A modified embedded-atom method interatomic potential for the fe-n system: A comparative study with the fec system. *Acta Materialia*, 54(17):4597–4607, 2006.
- [36] J.R.G. da Silva and R.B. McLellan. Diffusion of carbon and nitrogen in b.c.c. iron. *Materials Science and Engineering*, 26(1):83–87, 1976.
- [37] J.H. Bott, H. Yin, S. Sridhar, and M. Auinger. Theoretical and experimental analysis of selective oxide and nitride formation in fe-al alloys. *Corrosion Science*, 91:37–45, 2015.
- [38] M. Nikolussi, A. Leineweber, and E.J. Mittemeijer. Nitrogen diffusion through cementite layers. *Philosophical Magazine*, 90(9):1105–1122, 2010.
- [39] B. Lawrence, C.W. Sinclair, and M. Perez. Carbon diffusion in supersaturated ferrite: a comparison of mean-field and atomistic predictions. *Modelling and Simulation in Materials Science and Engineering*, 22(6):065003, 2014.
- [40] J. Aufrecht, A. Leineweber, J. Foct, and E.J. Mittemeijer. The structure of nitrogen-supersaturated ferrite produced by ball milling. *Philosophical Magazine*, 88(12):1835–1855, 2008.
- [41] S. DeWaele, K. Lejaeghere, E. Leunis, L. Duprez, and S. Cottenier. A first-principles reassessment of the fe-n phase diagram in the low-nitrogen limit. *Journal of Alloys and Compounds*, 775:758–768, 2019. ISSN 0925-8388.
- [42] H.A. Wriedt, N.A. Gokcen, and R.H. Nafziger. The fe-n (iron-nitrogen) system. *Bulletin of Alloy Phase Diagrams*, 8(4):355–377, 1987.
- [43] F. Ye, K. Tong, Y.K. Wang, Z. Li, and F. Zhou. First-principles study of interaction between vacancies and nitrogen atoms in fcc iron. *Computational Materials Science*, 149:65–72, 2018.

Appendix A. FCC 1 → 1 jump

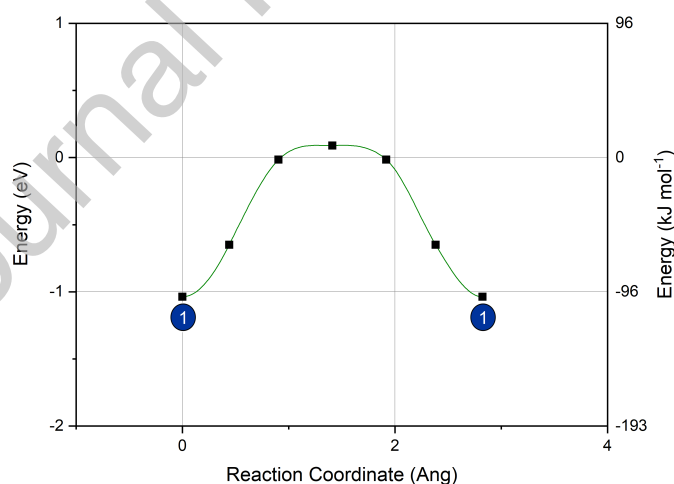


Figure A.9: The energy of an interstitial nitrogen atom in non-magnetic FCC iron relative to a nitrogen atom in the gas state, as it transitions between symmetrical octahedral positions which are first nearest neighbours to a vacancy. The process used to obtain the reference energy of nitrogen gas is detailed in Karimi and Auinger [3].

Figure A.9 shows the minimum energy path for a 1 → 1 jump of nitrogen in a FCC lattice, and a graphical representation of the jump in a FCC supercell is given in figure 1. The $E_{v(1 \rightarrow 1)}^N$ energy barrier was found to be $108.8 \text{ kJ mol}^{-1}$. $E_{v(1 \rightarrow 1)}^N$ is far smaller than all the other FCC energy barriers (see table 2), meaning that the 1 → 1 jump

rate $r_{v(1 \rightarrow 1)}^N$ is many orders of magnitude larger than the other jump rates. Moreover, the large $E_{v(1 \rightarrow 2)}^N = 252.7 \text{ kJ mol}^{-1}$ energy barrier ensures with high statistical certainty that many $1 \rightarrow 1$ jumps are repeated in succession before a nitrogen atom leaves a vacancy. At equilibrium, the random walk followed by each nitrogen atom which jumps between first nearest neighbour (FNN) positions to a vacancy in an arbitrary time interval is constrained to a finite domain. The finite domain ensures that, for any time interval where a nitrogen atom performs successive $1 \rightarrow 1$ jumps, every starting and ending position is equally likely. Hence, the mean squared displacement (MSD) (see equation 6) is constant with respect to a sequence of repeated $1 \rightarrow 1$ jumps over time. If the system is restricted to only $1 \rightarrow 1$ jumps, the theoretical value of the MSD is the expected value over all the possible squared displacements. There are a total of 36 squared displacements which the nitrogen atom can achieve in each coordinate dimension while restricted to FNN positions around a vacancy. 18 of the possible displacements are zero, 16 are $(\frac{a}{2})^2$ and two are a^2 . Hence, the MSD contribution at equilibrium is

$$\mu_{1 \rightarrow 1} = 3 \times \frac{16(\frac{a}{2})^2 + 2a^2}{36} = \frac{a^2}{2}. \quad (\text{A.1})$$

The lattice parameter a for γ Fe is given by the expression $a = 3.544 + 0.0000856T$ where T is the temperature [32]. For example, using equation A.1 for $T = 500 \text{ K}$, the equilibrium contribution of repeated $1 \rightarrow 1$ jumps to the MSD is 6.43 \AA^2 . Figure A.10 shows the effect of the $1 \rightarrow 1$ jump on the MSD in KMC simulations. At each temperature considered, the MSD fluctuates about the theoretical value implied by restricting the nitrogen atom to only FNN positions. The large $r_{v(1 \rightarrow 1)}^N$ rate means that the vast majority of KMC steps consist of repeated $1 \rightarrow 1$ jumps. Hence, a simulation with $1 \rightarrow 1$ jumps included requires orders of magnitude more KMC steps to reach equilibrium. The dashed lines in figure A.10 show that the MSD approaches the expected linear relationship with time, in the same number of KMC steps, if $1 \rightarrow 1$ jumps are omitted from the simulation.

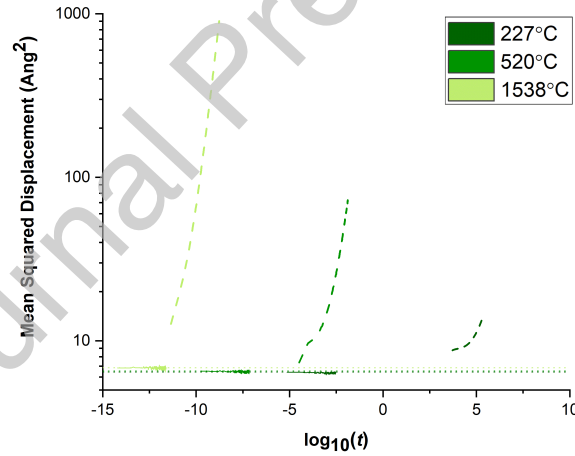


Figure A.10: Traces of the mean squared displacement of nitrogen atoms over time t in non-magnetic FCC iron with a vacancy concentration of 10 at.% and interstitial nitrogen concentration of 1 at.%. Solid lines represent trajectories where first nearest neighbour jumps for nitrogen around a vacancy are included in Kinetic Monte Carlo (KMC) simulations, and dashed lines represent trajectories where such jumps are omitted. Each of the six traces shown comprise of 250000 KMC steps. The dotted lines show the theoretical contribution to the mean squared displacement from repeated first nearest neighbour jumps of nitrogen around a vacancy at equilibrium.

It is not computationally viable to determine the impact of the $1 \rightarrow 1$ jump on the diffusion coefficient of nitrogen through direct calculation, because the $1 \rightarrow 1$ jump creates poor convergence behaviour in KMC. Rather, upper bounds are derived for its impact under the considered conditions in this work. Denote the MSD of a single nitrogen atom $\mu(t)$ at time t . At equilibrium, the MSD is linear with respect to time with a constant gradient. Thus, in equal-length time intervals, the MSD's are also equal. That is,

$$\mu(t) = \mu(t - k) + \mu(k) \quad (\text{A.2})$$

for any $t \geq k \geq 0$. Let $0 \leq t_{\text{enter}}^0 \leq t_{\text{exit}}^0 < t_{\text{enter}}^1 \leq t_{\text{exit}}^1 < \dots < t_{\text{enter}}^m \leq t_{\text{exit}}^m \leq t$ represent the (possibly zero) distinct times that the nitrogen atom enters/exits a vacancy. The $[t_{\text{enter}}^i, t_{\text{exit}}^i]$ interval spans the time where the nitrogen atom is in FNN positions to a vacancy. The $1 \rightarrow 1$ jump repeatedly occurs in the interval, with the last one completing at time t_{exit}^i . Denote the total time the nitrogen spends in FNN positions as $t_v = \sum_{i=0}^{i=m} t_{\text{exit}}^i - t_{\text{enter}}^i$. Using equation A.2, the MSD is

$$\mu(t) = |x(t) - x(0)|^2 = \underbrace{|x(t - t_v) - x(0)|^2}_{\text{all other jumps}} + \underbrace{\sum_{i=0}^{i=m} |x(t_{\text{exit}}^i) - x(t_{\text{enter}}^i)|^2}_{1 \rightarrow 1 \text{ jumps only}}. \quad (\text{A.3})$$

Where $x(t)$ denotes the location of the nitrogen atom at time t . At equilibrium, $m \leq 1 + r_{v(1 \rightarrow 2)}^N t$ in equation A.3, because a $1 \rightarrow 2$ jump must occur before each new unique vacancy entry time. Moreover, because nitrogen is restricted to a single vacancy in each interval, the value of $\frac{\sum_{i=0}^{i=m} |x(t_{\text{exit}}^i) - x(t_{\text{enter}}^i)|^2}{m}$ approaches $\frac{a^2}{2}$ (see equation A.1) as $m \rightarrow \infty$. Hence,

$$\begin{aligned} \sum_{i=0}^{i=m} |x(t_{\text{exit}}^i) - x(t_{\text{enter}}^i)|^2 &= m \frac{\sum_{i=0}^{i=m} |x(t_{\text{exit}}^i) - x(t_{\text{enter}}^i)|^2}{m} \leq (1 + r_{v(1 \rightarrow 2)}^N t) \frac{\sum_{i=0}^{i=m} |x(t_{\text{exit}}^i) - x(t_{\text{enter}}^i)|^2}{m} \\ \Rightarrow \sum_{i=0}^{i=\infty} |x(t_{\text{exit}}^i) - x(t_{\text{enter}}^i)|^2 &\leq (1 + r_{v(1 \rightarrow 2)}^N t) \frac{a^2}{2} \end{aligned} \quad (\text{A.4})$$

Combining equations 7, A.3 and A.4, and noting that $m \rightarrow \infty$ as $t \rightarrow \infty$

$$\begin{aligned} D(t) &= \lim_{t \rightarrow \infty} \frac{|x(t - t_v) - x(0)|^2}{6t} + \lim_{t \rightarrow \infty} \frac{\sum_{i=0}^{i=m} |x(t_{\text{exit}}^i) - x(t_{\text{enter}}^i)|^2}{6t} \\ &\leq \lim_{t \rightarrow \infty} \frac{|x(t - t_v) - x(0)|^2}{6t} + \lim_{t \rightarrow \infty} \frac{a^2(1 + r_{v(1 \rightarrow 2)}^N t)}{12t} \\ &= \lim_{t \rightarrow \infty} \frac{|x(t - t_v) - x(0)|^2}{6t} + \frac{a^2 r_{v(1 \rightarrow 2)}^N}{12}. \end{aligned} \quad (\text{A.5})$$

In this work, the diffusion coefficient is approximated by the left hand side term of equation A.5, by omitting the $1 \rightarrow 1$ jump from KMC simulations. Over all the conditions considered, the right hand side term is generally small compared to the left hand side term, meaning that the error caused by the approximation is small. Figure A.11 shows the maximum error by using equation A.5 to compute the maximum difference in the diffusion coefficient. For any vacancy concentration smaller than 1 at.%, the error is negligible. The only conditions where the error margin of 0.05 for KMC simulations (see section 2.2.2) are surpassed is when the vacancy concentration is 10 at.% and the temperature is over 900°C. The upper bound set by equation A.4 is generous, because $r_{v(1 \rightarrow 2)}^N t$ may be significantly larger than the rate that nitrogen visits new vacancies. Hence, the potential magnitude of error is insufficient to justify the vastly higher computational cost to include the $1 \rightarrow 1$ jump in KMC simulations.

Appendix B. Piecewise Log-Linear Interpolation

Piecewise log-linear interpolation is applied in this work to approximate the diffusion coefficient between two parameters when the other parameters are fixed. For example, at fixed T and c_{N_m} , let l index a sorted set of all the c_{v_l} where $c_{N_l} = c_{N_m}$. Then for any c_v with $c_{v_l} < c_v < c_{v_{l+1}}$, $\log(D^s(T, c_v, c_{N_m})) = B + A \log(c_v)$, where A and B define the line which joins $(\log(c_{v_l}), \log(D^s(T, c_{N_m}, c_{v_l})))$ and $(\log(c_{v_{l+1}}), \log(D^s(T, c_{N_m}, c_{v_{l+1}})))$.

Appendix C. Simulated Diffusion Data Plots

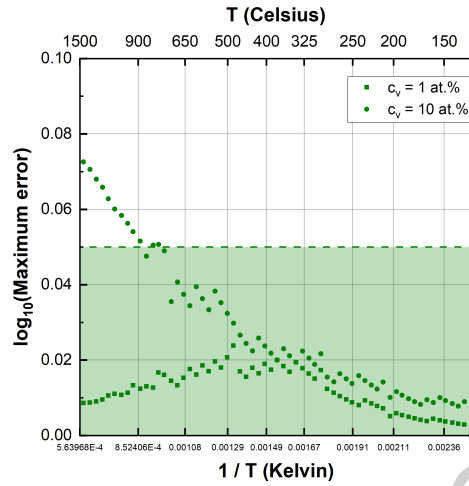


Figure A.11: Maximum error in the calculated diffusion coefficient of nitrogen in non-magnetic FCC iron, if first nearest neighbour jumps for nitrogen around a vacancy are omitted from Kinetic Monte Carlo simulations. The vacancy concentration of iron is denoted by c_v . The area under the dashed line shows where the error is smaller than the chosen convergence criteria for KMC simulations.

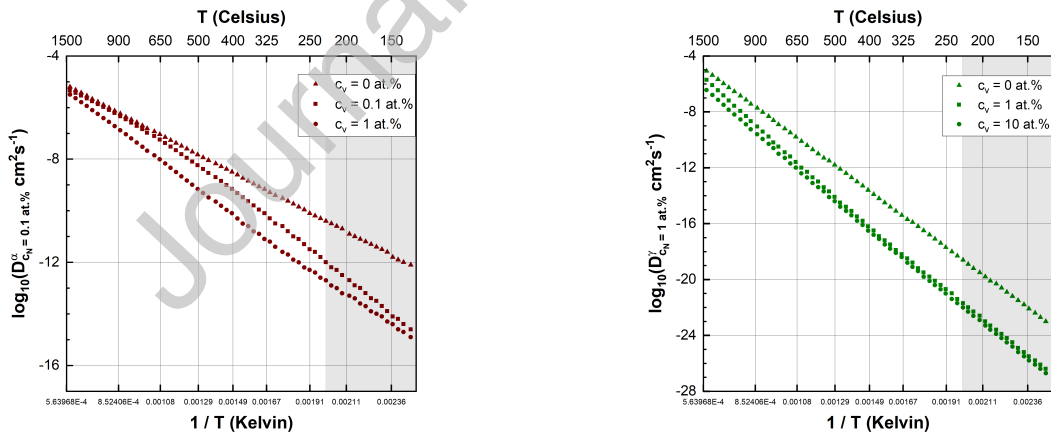


Figure C.12: The diffusion coefficient of nitrogen in α iron (red, top) and γ iron (green, bottom) with interstitial nitrogen concentrations of 0.1 at.% and 1 at.% respectively. The vacancy concentration of the iron is denoted by c_v . The data points represent converged data from Kinetic Monte Carlo simulations as detailed in the text. The grey shading indicates that the data points are extrapolated using a linear fit to the two closest calculated points.

Declaration of Competing Interest

The authors declare that they have no known competing financial interests or personal relationships that could have appeared to influence the work reported in this paper.

Journal Pre-proof